Orientational order in self-assembled nanocrystal superlattices

Zhaochuan Fan and Michael Grünwald*

Department of Chemistry, University of Utah, Salt Lake City, 84112 Utah, USA

michael.gruenwald@utah.edu

Abstract.

Self-assembly of nanocrystals into functional materials requires precise control over nanoparticle interactions in solution, which are dominated by organic ligands that densely cover the surface of nanocrystals. Recent experiments have demonstrated that small truncated-octahedral nanocrystals can self-assemble into a range of superstructures with different translational and orientational order of nanocrystals. The origin of this structural diversity remains unclear. Here, we use molecular dynamics computer simulations to study the self-assembly of these nanocrystals over a broad range of ligand lengths and solvent conditions. Our model, which is based on a coarse-grained description of ligands and solvent effects, reproduces the experimentally observed superstructures, including recently observed superlattices with partial and short-ranged orientational alignment of nanocrystals. We show that small differences in nanoparticle shape, ligand length and coverage, and solvent conditions can lead to markedly different self-assembled superstructures due to subtle changes in the free energetics of ligand interactions. Our results rationalize the large variety of different reported superlattices self-assembled from seemingly similar particles and can serve as a guide for the targeted self-assembly of nanocrystal superstructures.

Introduction.

This paper is concerned with the computational prediction of superlattices obtained by self-assembly of small nanocrystals (NCs), including popular NCs made from semiconductors materials (PbSe, PbS, Si, etc.) and gold. These nanoparticles typically have shapes resembling truncated octahedra and are covered with organic ligands (e.g., oleic acid).[1] Superstructures assembled from this class of nanoparticles show a surprisingly large variability from experiment to experiment,[2] including face-centered cubic (fcc),[3–6] body-centered cubic (bcc),[7,8] and body-centered tetragonal (bct) lattices.[9] The nanoparticles in these superlattices can be either rotationally disordered,[8,10] aligned with respect to symmetry axes of the superlattice,[5,7,9,10] or can adopt complex orientational patterns.[3,4,11,12] These different experimental outcomes have been correlated with a range of driving forces, including NC shape,[13] ligand interactions,[10] van der Waals[14,15] and dipole-dipole interactions[16,17] between nanoparticle cores, interactions with a substrate or interface,[7,18] and solvent quality.[19,20] Since the relative strength of these forces and the details of particle shape and ligand configurations are difficult to quantify in experiment, few reliable guiding principles have been developed that allow rationalizing or predicting the large number of different self-assembled structures.

In this work, we focus on the role played by surface-bound ligands in determining the structure of self-assembled superlattices. In solution, and in the dried superlattice, NCs primarily interact via ligands. For NCs with sizes of a few nanometers, straightforward estimates show that van der Waals forces between typical ligands (e.g., oleic acid) are much stronger than core-core interactions.[21] Ligand interactions are complex[22] and have been the subject of several computational[23–33] and experimental studies:[19] Ligands have been used to rationalize the equilibrium distances and thermodynamic stabilities of NCs in binary superlattices,[34,35] and have been exploited to steer self-assembly of NCs towards different superlattices.[13,29,36]

Interactions between ligands, and thus self-assembly outcomes, strongly depend on solvent conditions. In recent work, Tisdale and coworkers have shown that NCs can undergo several structural transformations as solvent is slowly evaporated.[7] Hanrath and coworkers have reported that different evaporation rates result in different superlattice symmetries, demonstrating that superlattices obtained through self-assembly are not always in equilibrium.[13] Computer simulations indeed confirm that interactions between ligands in the dried state are so strong that collective rearrangements of NCs are highly unlikely at room temperature.[25,37] To predict self-assembly outcomes, interactions between ligands under partly solvated conditions therefore need to be considered.

Simulating NC superlattices.

In this work, we use a coarse-grained molecular model of NCs and ligands to enable simulations that can access the time and length scales of superlattice assembly and transformation. Nanocrystals are modeled as rigid bodies with cuboctahedral or truncated octahedral shape (see Fig. 1a) and diameters of approximately 6 nm. Interactions between NC cores are neglected throughout this work, as these forces are typically much weaker than ligand interactions for small NCs (see Supp. Discussion and Supp. Fig. S1). Alkyl ligands are modeled as polymers of coarse-grained beads, each representing groups of four heavy atoms, as illustrated in Fig. 1b. Prototypical oleic acid ligands comprised of 18 carbon atoms (referred to as C_{18} ligands in the following) are represented here as polymers of 5 coarse-grained beads. Interaction parameters for ligand beads are taken from the MARTINI force field.[38] (All force field and simulations details are described in the Methods section and Supp. Methods.) Ligands are grafted to NC surfaces with different densities: $\{100\}_{NC}$ surfaces have ligand coverage of 1/35 Å^{-2}, $\{111\}_{NC}$ surfaces have higher coverage of 1/30 Å^{-2} (see Fig. 1a). These surface densities are consistent with a recent DFT study of oleic acid molecules on PbS NCs.[39]

An explicit representation of solvent molecules is exceedingly expensive in simulations of many NCs. We therefore approximate effects of varying solvent quality and solvent content by modifying attractive interactions between ligands, which are strong in air or in a bad solvent, but much weaker in good solvents.[40,41] To represent these trends and model different solvation environments of ligands, we introduce a "solvent parameter" s ($0 \leq s \leq 1$) that scales the attractive part of the ligand pair potential (see Supp. Fig. S2). While $s = 1$ represents ligands in air (*i.e.*, the dried state of a self-assembled superlattice), values of $s < 1$ represent solvents of different quality and abundance. Figure 1b illustrates typical ligand configurations of a NC covered with ligands comprising 18 carbon atoms at different values of s. With increasing s, ligand shells contract and interactions between nanoparticles become stronger. In Supp. Fig. S3, we compare potentials of mean force (PMF) for two NCs at different values of s with PMF obtained using *explicit* solvents of different quality. The trends observed with increasing s qualitatively match trends for decreasing quality of the explicit solvent. A continuous change of s from zero to one in molecular dynamics (MD) simulations therefore serves as a coarse way to model changing solvent environments during anti-solvent addition or solvent evaporation. As discussed below, we have verified in one case that computationally strenuous simulations using explicit solvent produce the same NC superlattices as the much more efficient implicit solvent model.
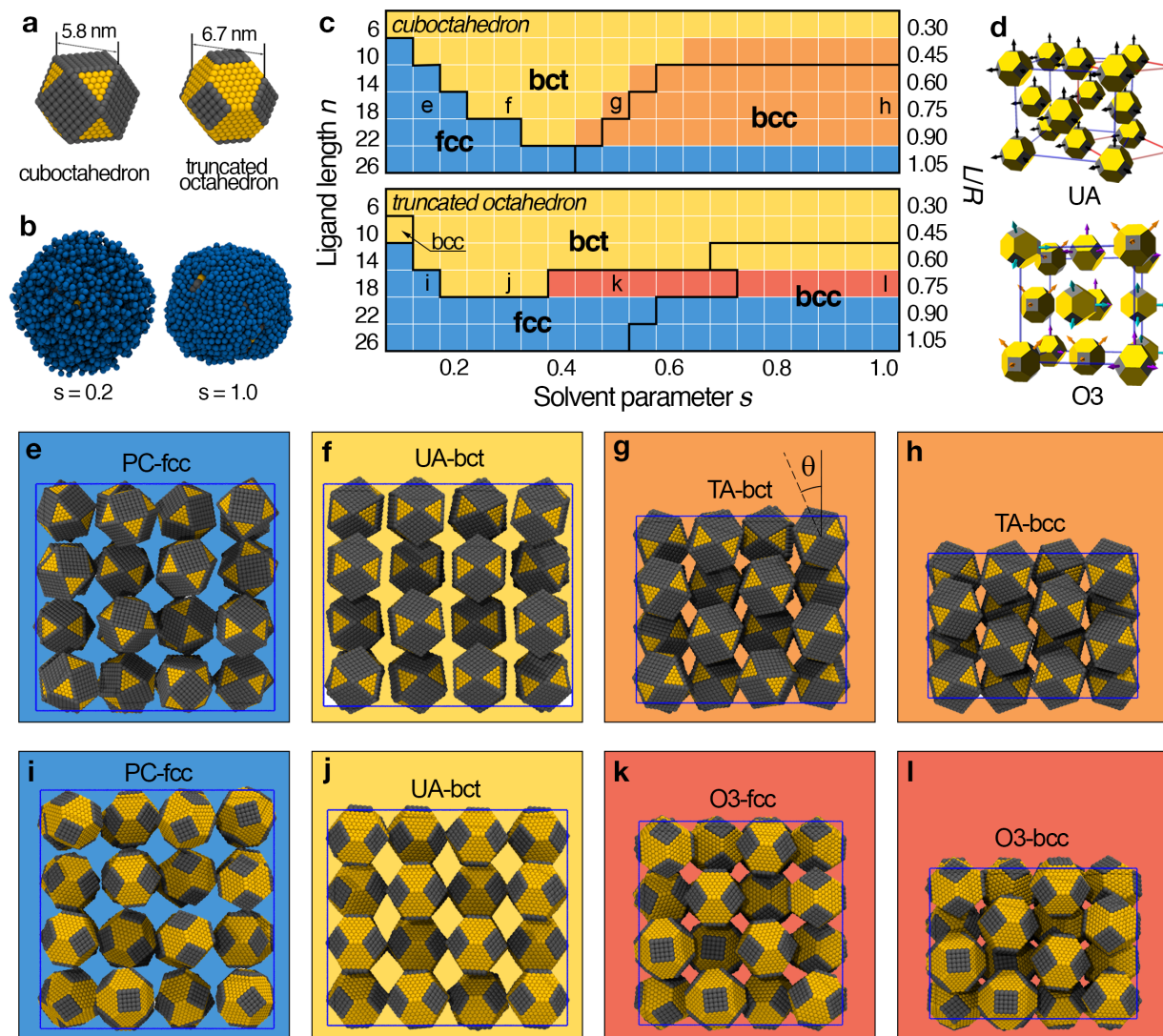
Figure 1. Structural diversity in NC superlattices. (a) Models of NC cores used in this work. Yellow and gray beads represent attachment points for ligands on the two different exposed surfaces; based on an atomistic lattice of sodium chloride type, yellow and gray beads indicate $\{111\}_{NC}$ and $\{100\}_{NC}$ facets, respectively. (b) Snapshots from MD simulations of isolated truncated octahedral NCs with C_{18} ligands at different values of the solvent parameter s. (c) Kinetic phase diagram of cuboctahedral (top) and truncated octahedral (bottom) NCs, as a function of ligand length (n is the number of carbon atoms, L the stretched ligand length, R the NC radius) and solvent parameter s. Black solid lines delimit lattices of different translational symmetry (fcc, bcc, and bct). Colors indicate different orientations of NCs, as explained in the text. Phase boundaries reflect midpoints of up- and downstroke transitions. (d) Schematic representation of the UA-bct (top) and O3-fcc (bottom) structures. Arrows indicate the $\langle 100 \rangle_{NC}$ directions of NCs. Differently colored arrows (orange, cyan, and purple) in O3-fcc indicate NCs with three distinct orientations. The blue and red lines indicate face-centered and body-centered unit cells, respectively. (e)-(l) Snapshots from MD simulations of 32 NCs (ligands not shown) at conditions corresponding to labels in panel (c).

Phase diagrams of NC superlattices.

Our model shows a rich phase behavior that depends sensitively on NC shape, ligand length, and solvation environment. In Fig. 1c, we present the kinetic phase diagrams of both NC shapes, which we determined by running long straightforward MD simulations at increasing and decreasing values of the solvent parameter s. In agreement with a large body of experimental work, we find superlattices with fcc, bct, and bcc symmetries. In addition to these different lattices, we observe four distinct types of orientational alignment of NCs on their lattice sites. Specifically, we observe plastic crystals with orientationally disordered NCs (referred to as "PC", blue regions in Fig. 1c), lattices with NCs that have uniform orientations aligned with the axes of the body-centered superlattice ("UA", yellow), as well as particles with uniform orientations that are tilted with respect to the lattice axes ("UT", orange). In the case of truncated octahedral NCs, we furthermore observe a phase with complex orientational order: NCs are not uniformly orientated but take on one of three distinct orientations ("O3", red). In the following, we discuss some of the features of the phase diagrams and compare them to experiments.

When covered with very short ligands (~6 carbons), NC with both shapes form UA-bct structures. Despite the short ligand length, the UA-bct structure does not match the structures found for hard truncated octahedra (bcc) and cuboctahedra (distorted simple cubic),[42–45] underscoring the relevance of ligand interactions even for very short ligands. Long ligands (~26 carbons or longer), on the other hand, effectively mask the polyhedral shapes of NCs cores. Both NC shapes investigated here show similar phase behavior when covered with long ligands: they transform from PC-fcc to PC-bcc structures when s is increased. The fact that nanoparticles with long ligands tend to form bcc structures has been the subject of several studies;[29,36,46] it contradicts the notion that NCs with long ligands behave like soft spheres and thus should form close-packed (fcc) structures. The preference for bcc has been first rationalized by Landman and coworkers.[29] Our simulations confirm these authors' results: The bcc structure is *energetically* favored over the fcc structure because ligands on second-nearest neighbor nanoparticles can strongly interact with each other in the bcc structure if ligands are long enough. In fact, we find that in bcc superlattices the space between NCs is completely filled with ligands. In these structures, NCs directly interact with 14 other NCs via their ligands, including the first and second nearest neighbors in the bcc lattice. In bct and fcc superlattices, on the other hand, substantial gaps in the ligand structure remain in the octahedral cavities of the fcc/bct structure, as illustrated in Fig. 2. Due to the presence of these gaps, which in experiments will be filled with solvent, NCs only directly interact with 12 other NCs. Upon solvent evaporation, these gaps are filled with ligands, providing a substantial energetic advantage for bcc structures, consistent with recent calorimetric measurements on PbSe superlattices.[2]
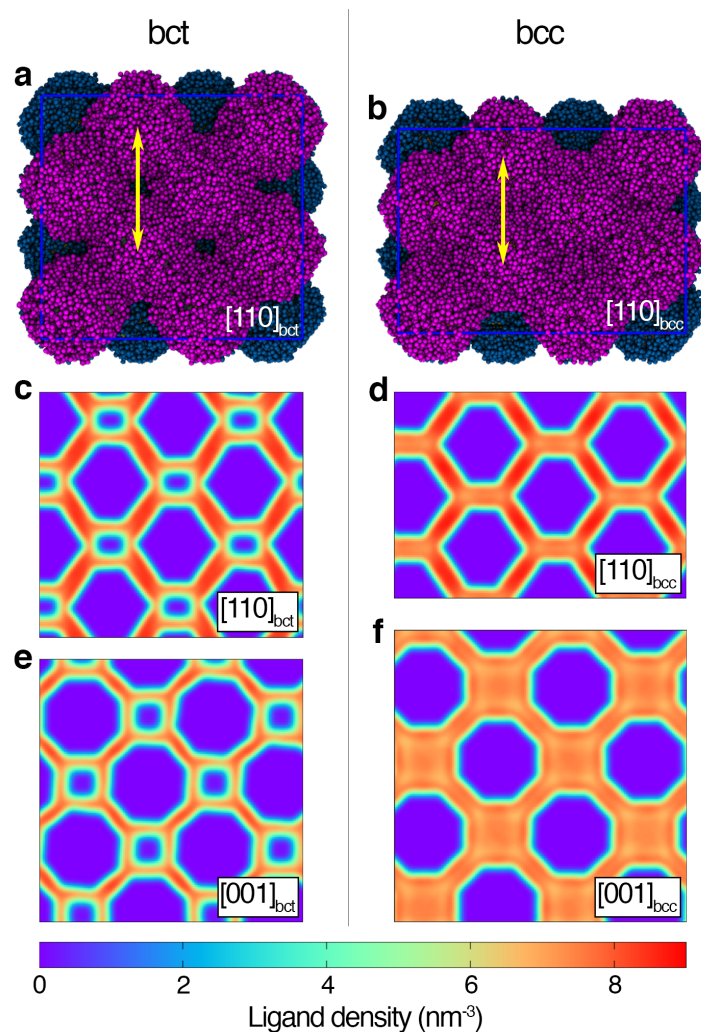
Figure 2. Ligand distributions in NC superlattices. (a)-(b) Snapshots from MD simulations of truncated octahedral NCs with C_{14} ligands at $s = 0.7$, in the UA-bct (a) and UA-bcc (b) structures. Systems are viewed along the $[110]_{bct/bcc}$ superlattice direction. NCs in two different $(110)_{bct/bcc}$ layers are colored dark blue and purple. In the bct structure, ligands do not extend all the way into the octahedral voids formed between second-nearest neighbor NCs. (One such pair is indicated by a yellow arrow.) In the bcc structure, these voids are occupied by ligands. (c)-(f) Average ligand density (in units of ligand beads per nm^3) in the UA-bct (left) and UA-bcc (right) structures, viewed along $[110]_{bct/bcc}$ (c-d) and $[001]_{bct/bcc}$ (e-f) superlattice directions.

The phase behavior of NCs is most sensitive to small variations of particle shape and solvent properties for intermediate ligand lengths (~18 carbons), which include oleic acid molecules most frequently used in experiments. Truncated octahedral NCs form a PC-fcc superlattice at small values of s and undergo a sharp transition to UA-bct when solvent is evaporated. Surprisingly, upon further solvent evaporation, NCs lose their orientational alignment again to form the O3-fcc superlattice (and eventually a O3-bcc structure). This progression of structures is illustrated in Fig. 1 i-l and in Supp. Movie 1. NCs in the O3-fcc structure align one of their $<100>_{NC}$ directions with one of three $<100>_{fcc}$ superlattice directions (see Fig. 1d, lower panel); the other two $<100>_{NC}$ directions are aligned with $<110>_{fcc}$ superlattice directions. This set of orientations ensures that all 12 nearest-neighbor contacts in the superlattice are face-to-face. The observation of the O3-fcc structure in our simulations confirms a recent series of experiments suggesting superlattices with NCs that are neither completely disordered orientationally, nor uniformly aligned.[3,4,11,12] Recently, Wang and coworkers suggested the existence of distinct fcc polymorphs with different sets of NC orientations in the unit cell.[4] Our simulations show that there is no such long-range correlation between the orientations of NCs. Instead, NCs can access all three orientations with similar probability and, in the presence of sufficiently good solvent, transitions between these orientations occur frequently on the simulation timescale (see Supp. Movie 1). In fact, the three orientations found in the O3-fcc are already foreshadowed in the rotational dynamics of NCs in the PC-fcc superlattice, where NCs display weak but noticeable preferences for the same three orientations (see Supp. Fig. 4).

To confirm that the occurrence of O3-fcc structure in our simulations is not an artifact of the implicit solvent model, we have performed a simulation of 4 NCs with C_{18} ligands in *explicit* octane solvent, which is slowly evaporated over a period of 30 μs (see Supp. Methods). As illustrated in Supp. Fig. S5, NCs in this simulation adopt a series of structures that includes O3-fcc and that is consistent with the sequence of superlattices obtained with the implicit solvent model. We note that in both implicit and explicit solvent simulations, the O3-fcc structure does not persist in the dried state (i.e., at $s = 1$) but is only observed in a partially solvated environment. This result is consistent with experimental reports of the O3-fcc structure, which is produced either through anti-solvent addition[3] or, most recently, through addition of excess ligands.[12] In both cases, solvent or ligand molecules likely remain trapped inside the NC superlattice, filling octahedral voids.[47] Indeed, fcc superlattices have been reported to develop cracks associated with release of solvent molecules when dried for extended periods of time after self-assembly.[48]

Superlattices with complex O3 orientations are only observed for truncated octahedral NCs in a narrow range of ligand lengths. NCs with modestly shorter ligands (or, equivalently, modestly larger core size), transform from PC-fcc to UA-bct and, finally, to UA-bcc at large values of s. This progression of structures,

the so-called Bain deformation, was recently reported by Hanrath and coworkers[13] and Tisdale and coworkers[7] with in-situ X-ray diffraction during controlled manipulation of solvent content and quality.

A modest change of particle shape from truncated-octahedral to cuboctahedral likewise results in a markedly different phase diagram. Phases with partial orientational order of NCs (O3) are not observed for cuboctahedra. As s is increased, we instead observe a transition from UA-bct to UT-bct and UT-bcc, as illustrated in Fig. 1e-h. The UT-bct and UT-bcc structures are characterized by NC orientations that are not aligned with, but uniformly tilted with respect to the superlattice axis. Specifically, a $[100]_{NC}$ direction forms an angle of approximately 20° with the corresponding $[100]_{bct}$ superlattice direction. Similar tilts have been observed for perfectly hard polyhedra with shapes close to the cuboctahedron.[43] However, experimental evidence for NCs with well-defined cuboctahedral shape is scarce. Korgel and coworkers have reported that large cuboctahedral Si NCs with C_{12} ligands ($L/R \approx 0.2$) form an fcc superlattice with aligned NC orientations.[5] Superlattices with tilted NCs have so far been observed experimentally only in the vicinity of a flat substrate.[7] However, we observe tilted NC superstructures for a wide range of ligand lengths, suggesting that these superlattices should be accessible in experiments if NC shape is indeed close to cuboctahedral.

Thermodynamic stability of superlattices with complex NC orientations.

In the remainder of this paper, we focus on identifying the thermodynamic driving forces for the formation of the O3-fcc superstructure. To this end, we have calculated Gibbs free energies of truncated octahedral particles with C_{18} ligands (see Methods) in the PC-fcc, UA-bct and O3-fcc structures as a function of s. In good agreement with our straightforward MD simulations, we find coexistence ($\Delta G = 0$) between the PC-fcc and UA-bct at $s \approx 0.20$, and between UA-bct and O3-fcc at $s \approx 0.36$, as shown in Fig. 3a. Decomposition of the free energy into enthalpic and entropic contributions shows that both transformations (PCC-fcc to UA-bct and UA-bct to O3-fcc) are energetically favorable and accompanied by a loss of entropy, consistent with the increasing strength of attractive ligand-ligand interactions. But while a decrease in entropy is evident from the freezing of rotational degrees of freedom during the PC-fcc to UA-bct transition, the loss of entropy during the transformation from UA-bct to O3-fcc is accompanied by a partial *disordering* of rotational degrees of freedom of NCs. To rationalize this counterintuitive result and identify the origin of the energetic contributions that drive this transition, we have analyzed changes in local ligand densities. We observe small but statistically significant differences between the UA-bct and O3-fcc structures, as illustrated in Fig. 3b. Compared to the UA-bct, ligands in the O3-fcc structure pack more densely on average and the volume of solvent-filled gaps in the superlattice is slightly larger (see Supp. Discussion); this increase in ligand density is directly linked to a decrease in average potential energy (Fig. 3c.). As evident

from Figs. 3b-c, the density increase and energy decrease stem mostly from the tails of ligands on $\{100\}_{NC}$ surfaces. Consistent with this result, interacting NCs in the O3-fcc structure on average have a slightly smaller $\{100\}_{NC}$ surface-to-surface distance (see Supp. Fig. S6). We thus conclude that the salient effect of the different NC orientations in the O3-structure is to compress ligands on $\{100\}_{NC}$ facets, enabling more favorable ligand interactions compared to the UA-bct structure.
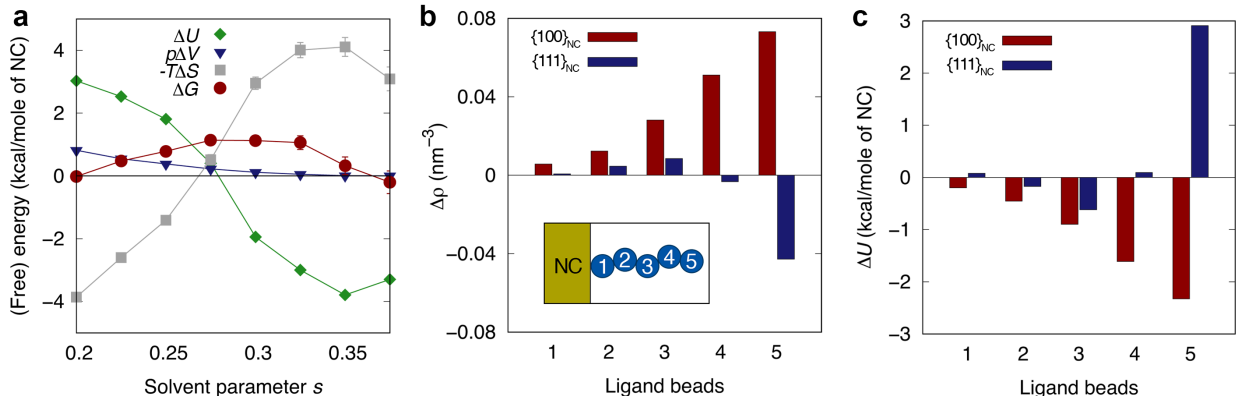

Figure 3. The O3-fcc structure is energetically stabilized by favorable interactions of ligands on $\{100\}_{NC}$ facets. (**a**) Contributions to the free energy difference $\Delta G = G_{bct} - G_{fcc} = \Delta U - T\Delta S + p\Delta V$ between UA-bct and O3-fcc superlattices of truncated octahedra with C_{18} ligands, as a function of the solvent parameter s. When not shown, errorbars are smaller than the symbol size. (**b**) Average local density differences $\Delta\rho = \rho_{fcc} - \rho_{bct}$ (see Methods) around ligand beads at $s = 0.35$. Separate data are shown for ligands at different locations along the ligand chain (labeled 1-5, see inset) and for ligands on $\{100\}_{NC}$ (red) and $\{111\}_{NC}$ (blue) facets. Ligands on $\{100\}_{NC}$ facets have larger average density in O3-fcc. (**c**) Average potential energy differences $\Delta U = U_{bct} - U_{fcc}$ of ligand beads at $s = 0.35$, labeled as in (b). Ligands on $\{100\}_{NC}$ facets are responsible for the lower potential energy of the O3-fcc structure.

Why are ligand shells preferentially compressed on $\{100\}_{NC}$ facets? In our NC models, we chose a smaller ligand coverage on $\{100\}_{NC}$ compared to $\{111\}_{NC}$ facets, in agreement with several experimental and computational studies.[39,49] Smaller ligand coverage results in a lower local ligand density and larger compressibility of ligands on $\{100\}_{NC}$ facets (see Supp. Fig. S6). This reasoning suggests that the thermodynamic stability of the O3-fcc structure should be sensitive to changes in ligand coverage (and thus compressibility of ligand shells) on $\{100\}_{NC}$ facets. To test this hypothesis, we have performed MD simulations of truncated octahedral NCs with C_{18} ligands with *increased* ligand coverage on $\{100\}_{NC}$ facets, equal to that on $\{111\}_{NC}$ facets. In these simulations, we do not observe the O3-fcc structure, but NCs directly transform from UA-bct to UA-bcc, as illustrated in Fig. 4a. By contrast, NCs with *decreased* ligand coverage on $\{100\}_{NC}$ facets

(Fig. 4c) do not adopt the UA-bct structure in simulations but transform from PC-fcc directly to O3-fcc. These results explain why the O3-fcc structure has so far only been observed for lead chalcogenide NCs and not, for instance, for gold NCs, which can be prepared with similar truncated octahedral shapes. Ligand coverage on gold NCs is typically larger that on PbS/PbSe NCs because of much stronger binding of ligands to gold surfaces.[50] Ligand coverage has been identified before as an important parameter for superlattice assembly;[10] it can be partially controlled in experiments by repeated precipitation or aging of particles, and through addition of excess ligands. The ligand coverages used in our simulations are likely close to maximum coverages achievable in experiments; actual coverages in experiments can be substantially lower, facilitating the observation of the O3-fcc structure in experiments.
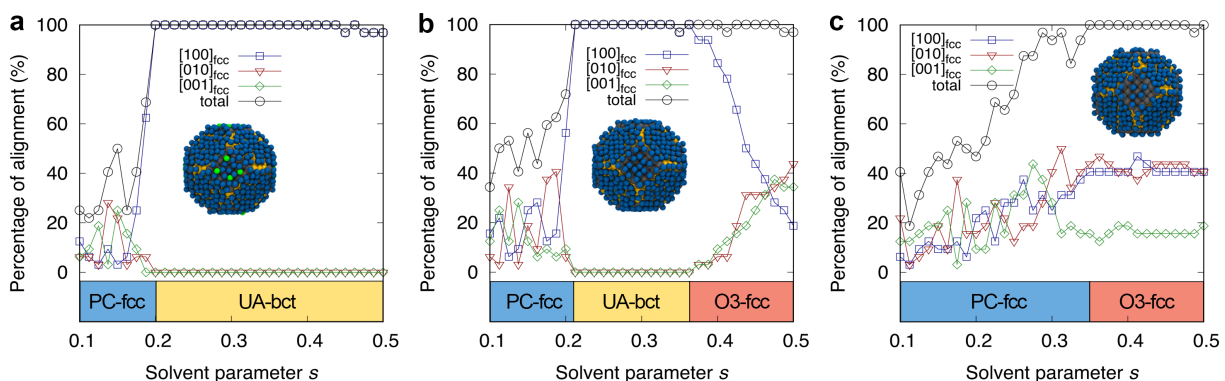

Figure 4. The O3-fcc structure is sensitive to changes in ligand coverage. Fraction of NCs that align one of three <100>$_{NC}$ directions with either the [100]$_{fcc}$ (blue squares), [010]$_{fcc}$ (red triangles), or [001]$_{fcc}$ (green diamonds) direction of the superlattice (see Methods). Data is shown for three MD simulations of truncated octahedral NCs with C_{18} ligands with different ligand coverage on {100}$_{NC}$ facets, as a function of the solvent parameter s. Insets show NC cores with attached ligand headgroups (blue). (Tails are not shown for clarity.) Additional ligands are shown in green color. (a) Four additional ligands have been added on each {100}$_{NC}$ surface to obtain a coverage of 1/30 Å^{-2}. (b) Original coverage of 1/35 Å^{-2} on {100}$_{NC}$ surfaces. (c) Nine ligands have been removed from each {100}$_{NC}$ surface to obtain a coverage of 1/54 Å^{-2}. Superlattices are assigned according to orientational alignment of NCs: small and transient alignment (PC-fcc), all NCs aligned along a single direction (UA-bct), and all NCs aligned, each in one of three different directions (O3-fcc). Nanocrystals are classified as "aligned", if the angle between NC and superlattice directions is smaller than 20°.

10

Conclusions.

The NC superlattices observed in this work are bulk equilibrium structures for different solvation environments that arise at different stages of a solvent evaporation experiments or for different solvent quality. If experimental systems of NCs can access these equilibrium states will depend on many factors including the solvent evaporation rate and the presence of interfaces or substrates. Non-equilibrium effects of solvent-evaporation,[51] for instance, have been neglected in this work. Our work reveals an extraordinary sensitivity of superlattice symmetry to changes in NC shape, ligand coverage, and solvent environment. In experiments, these parameters are often only partially controlled, which explains the broad range of different reported superlattices. Our analysis shows that self-assembly of superlattices is largely controlled by the spatial distribution of ligands in the spaces between NCs. The size of solvent-filled cavities in the superlattice and different local compressibility of ligand shells are important determinants of the thermodynamic stability of NC superlattices. Existing analytical models based on ligand density[36] can potentially be modified to take these parameters into account. Experimentally, enhanced characterization and control of ligand coverage on different NC facets will open the door to precisely targeted superlattice self-assembly.

Methods

Implicit solvent model. NC cores were modeled as hollow rigid bodies with truncated octahedral or cuboctahedral shape. Ligands were attached to the surface of NCs via harmonic bonds. The MARTINI force field[38] was used to describe ligand-ligand interactions. To implicitly include solvent effects, non-bonded MARTINI interactions were modified as follows:

$$u(r; s) = \begin{cases} u_{\mathrm{LJ}}(r) + (1 - s)\varepsilon, & r \leq 2^{1/6}\sigma \\ s\, u_{\mathrm{LJ}}(r), & 2^{1/6}\sigma < r \leq r_{\mathrm{cut}} \end{cases}$$

Here, $u_{\mathrm{LJ}}(r) = 4\varepsilon[(\sigma/r)^{12} - (\sigma/r)^6]$ is the standard Lennard-Jones (LJ) potential, ε and σ are interaction parameters taken from the MARTINI force field, and s is the solvent parameter. The value of s ($0 < s < 1$) sets the strength of attractive LJ interactions relative to the original MARTINI values, which describe interactions in vacuum (i.e., $s = 1$). The ligand-ligand pair potential is plotted for different values of s in Supp. Fig. S2. Model details and force-field parameters are specified in the Supp. Methods and Supp. Table S1.

Molecular dynamics simulations. All MD simulations were carried out with LAMMPS.[52] Simulations of NC superlattices were performed in the isothermal-isobaric (NpT) ensemble with a time step of 10 fs. Temperature (300 K) and pressure (1 atm) were controlled by a Langevin thermostat and a Berendsen barostat,

respectively, as implemented in LAMMPS. Simulations were initialized from an fcc superlattice of 32 NCs in a periodically replicated cubic box and equilibrated at $s = 0$ for 200 ns. To obtain kinetic phase diagrams shown in Fig. 1c, two MD simulations were performed for each NC system, with increasing and decreasing values of s. Hysteresis was observed near transition points between different superlattices (see Supp. Tables S2 and S3); Transition points indicated in Fig. 1c are average values of the up- and downstroke transition points. The solvent parameter s was changed during simulations with rates that varied between 0.0125 μ s^{-1} and 0.5 μ s^{-1}. In general, lower rates were used for systems with shorter ligands, and for truncated octahedral NCs with C_{18} ligands in the stability region of the O3-fcc structure.

Free energy calculations. We used the lattice-coupling-expansion method by Meijer and coworkers[53,54] to calculate free energy differences between UA-bct and O3-fcc superlattices of truncated octahedral NCs with C_{18} ligands at different values of s. Calculations were performed in two stages. In the first stage, the geometrical centers of NC cores were coupled to their lattice sites (which were determined in preliminary MD simulations) with harmonic springs (spring constant $\alpha = 0.1$ kcal/(mol Å^2)). To constrain the orientational degrees of freedom of NCs, six additional points on NC cores were harmonically coupled to anchor sites arranged in an octahedral geometry around lattice sites. Equilibrium sampling at constant NVT was carried out for 20 different values of spring constants $\lambda\alpha$, where $\lambda = 0, 0.05, 0.1, ... , 1.0$. Systems were simulated for 30 ns at each value of λ, with the last 10 ns used for sampling. The free energy change ΔF_{spr} due to the harmonic coupling was calculated numerically according to

$$\Delta F_{\text{spr}} = \int_0^1 d\lambda \left\langle \sum_{i=1}^{N_s} \frac{\alpha}{2} \left(\vec{r}_i - \vec{r}_{i,0} \right)^2 \right\rangle_\lambda ,$$

where N_s is the total number of springs, $\vec{r}_i$ is the position of the attachment point of spring i on a NC, $\vec{r}_{i,0}$ is the corresponding fixed anchor site position, and $\langle ... \rangle_\lambda$ denotes an equilibrium average at a particular value of λ. In a second stage, the NC superlattice was expanded gradually and uniformly by scaling the positions of spring anchor points, $\vec{r}_{i,0}(\gamma) = \gamma \vec{r}_{i,0}$. The superlattice was expanded until NCs did not interact with each other ($\gamma = 1.35$). The lattice expansion was performed in 30 steps, for $\gamma = 1.0, 1.005, 1.01, ...,1.05, 1.06, 1.07, ..., 1.15, 1.17, 1.19, ..., 1.35$. Systems were simulated for 50 ns at each value of γ, with the last 20 ns used for sampling. The free energy change ΔF_{exp} due to lattice expansion was calculated numerically according to

$$\Delta F_{\text{exp}} = \int_1^{1.35} d\gamma \left\langle \sum_{i,j} \frac{\partial u(r_{ij}; s)}{\partial r_{ij}} \frac{\partial r_{ij}}{\partial \gamma} \right\rangle_\gamma ,$$

where $u(r;s)$ is the implicit solvent pair potential defined above, and the sum extends over all pairs of beads on *different* NCs. The Gibbs free energy of the NC superlattice is $G = F_{\text{ref}} - \Delta F_{\text{spr}} - \Delta F_{\text{exp}} + pV$, where F_{ref} is the free energy of the expanded reference state of non-interacting NCs, and V is the average volume of the NC system at a pressure of $p = 1$ atm. The Gibbs free energy difference ΔG between the O3-fcc and UA-bct superlattices was thus calculated as

$$\Delta G = G^{\text{O3-fcc}} - G^{\text{UA-bct}} = \Delta F_{\text{spr}}^{\text{UA-bct}} - \Delta F_{\text{spr}}^{\text{O3-fcc}} + \Delta F_{\text{exp}}^{\text{UA-bct}} - \Delta F_{\text{exp}}^{\text{O3-fcc}} + p\left(V^{\text{O3-fcc}} - V^{\text{UA-bct}}\right).$$

Ligand density analysis. To characterize local ligand density in a continuous fashion, we represent each ligand bead by a Gaussian density profile,

$$\phi(r) = (2\pi\xi^2)^{-\frac{3}{2}} e^{-\frac{r^2}{2\xi^2}},$$

where r is the distance from the center of the bead and $\xi = 3.5$ Å is a smearing parameter whose value was chosen as a compromise between spatial resolution and smoothness of the density profile. The ligand density at a given point in space is then calculated by summing up contributions from all ligand beads within a distance of 3ξ. Heatmaps of average ligand density, as shown in Fig. 2, were calculated by sampling ligand density on a 1.5×1.5 Å^2 grid along particular cross-sections of the simulation box. Local densities of ligand beads on different facets and in different superlattices, used to calculate density differences shown in Fig. 3, were calculated as time averages of ligand density at the positions of particular ligand beads.

Acknowledgements

Author contributions

Z.F. and M.G. conceived the study, analyzed data, and wrote the manuscript. Z.F. performed all simulations.

References

1.	Panthani, M. G., Hessel, C. M., Reid, D., Casillas, G., José-Yacamán, M. & Korgel, B. A. Graphene-supported high-resolution TEM and STEM imaging of silicon nanocrystals and their capping ligands. *J. Phys. Chem. C* **116,** 22463–22468 (2012).

2.	Quan, Z., Wu, D., Zhu, J., Evers, W. H., Boncella, J. M., Siebbeles, L. D. a, Wang, Z., Navrotsky, A. & Xu, H. Energy landscape of self-assembled superlattices of PbSe nanocrystals. *Proc. Natl. Acad. Sci.* **111,** 9054–9057 (2014).

3.	Simon, P., Rosseeva, E., Baburin, I. A., Liebscher, L., Hickey, S. G., Cardoso-Gil, R., Eychmüller, A., Kniep, R. & Carrillo-Cabrera, W. PbS-Organic Mesocrystals: The Relationship between Nanocrystal Orientation and Superlattice Array. *Angew. Chemie Int. Ed.* **51,** 10776–10781 (2012).

4.	Li, R., Bian, K., Hanrath, T., Bassett, W. A. & Wang, Z. Decoding the superlattice and interface structure of truncate PbS nanocrystal-assembled supercrystal and associated interaction forces. *J. Am. Chem. Soc.* **136,** 12047–12055 (2014).

5.	Yu, Y., Lu, X., Guillaussier, A., Voggu, V. R., Pineros, W., De La Mata, M., Arbiol, J., Smilgies, D. M., Truskett, T. M. & Korgel, B. A. Orientationally Ordered Silicon Nanocrystal Cuboctahedra in Superlattices. *Nano Lett.* **16,** 7814–7821 (2016).

6.	Nagaoka, Y., Chen, O., Wang, Z. & Cao, Y. C. Structural Control of Nanocrystal Superlattices Using Organic Guest Molecules. *J. Am. Chem. Soc.* **134,** 2868–2871 (2012).

7.	Weidman, M. C., Smilgies, D.-M. M. & Tisdale, W. A. Kinetics of the self-assembly of nanocrystal superlattices measured by real-time in situ X-ray scattering. *Nat. Mater.* **15,** 775–781 (2016).

8.	Goubet, N., Albouy, P. A., Thompson, A. & Pileni, M. P. Polymorphism in nanoparticle-based crystals depending upon their single or polycrystalline character. *CrystEngComm* **18,** 6166–6175 (2016).

9.	Novák, J. J., Banerjee, R., Kornowski, A., Jankowski, M., André, A., Weller, H., Schreiber, F. & Scheele, M. Site-Specific Ligand Interactions Favor the Tetragonal Distortion of PbS Nanocrystal Superlattices. *ACS Appl. Mater. Interfaces* **8,** 22526–22533 (2016).

10.	Choi, J. J., Bealing, C. R., Bian, K., Hughes, K. J., Zhang, W., Smilgies, D. M., Hennig, R. G., Engstrom, J. R. & Hanrath, T. Controlling nanocrystal superlattice symmetry and shape-anisotropic interactions through variable ligand surface coverage. *J. Am. Chem. Soc.* **133,** 3131–3138 (2011).

11.	Simon, P., Bahrig, L., Baburin, I. A., Formanek, P., Röder, F., Sickmann, J., Hickey, S. G., Eychmüller, A., Lichte, H., Kniep, R. & Rosseeva, E. Interconnection of nanoparticles within 2D superlattices of PbS/oleic acid thin films. *Adv. Mater.* **26,** 3042–3049 (2014).

12.   Bian, K., Li, R. & Fan, H. Controlled Self-Assembly and Tuning of Large PbS Nanoparticle Supercrystals. *Chem. Mater.* acs.chemmater.8b02691 (2018). doi:10.1021/acs.chemmater.8b02691

13.   Bian, K., Choi, J. J., Kaushik, A., Clancy, P., Smilgies, D. M. & Hanrath, T. Shape-anisotropy driven symmetry transformations in nanocrystal superlattice polymorphs. *ACS Nano* **5,** 2815–2823 (2011).

14.   Abécassis, B., Testard, F. & Spalla, O. Gold Nanoparticle Superlattice Crystallization Probed In Situ. *Phys. Rev. Lett.* **100,** 115504 (2008).

15.   Sigman, M. B., Saunders, A. E. & Korgel, B. A. Metal Nanocrystal Superlattice Nucleation and Growth. *Langmuir* **20,** 978–983 (2004).

16.   Talapin, D. V., Shevchenko, E. V., Murray, C. B., Titov, A. V. & Král, P. Dipole−Dipole Interactions in Nanoparticle Superlattices. *Nano Lett.* **7,** 1213–1219 (2007).

17.   Bertolotti, F., Dirin, D. N., Ibáñez, M., Krumeich, F., Cervellino, A., Frison, R., Voznyy, O., Sargent, E. H., Kovalenko, M. V., Guagliardi, A. & Masciocchi, N. Crystal symmetry breaking and vacancies in colloidal lead chalcogenide quantum dots. *Nat. Mater.* **15,** 987–994 (2016).

18.   Geuchies, J. J., van Overbeek, C., Evers, W. H., Goris, B., de Backer, A., Gantapara, A. P., Rabouw, F. T., Hilhorst, J., Peters, J. L., Konovalov, O., Petukhov, A. V., Dijkstra, M., Siebbeles, L. D. A., van Aert, S., Bals, S. & Vanmaekelbergh, D. In situ study of the formation mechanism of two-dimensional superlattices from PbSe nanocrystals. *Nat. Mater.* **15,** 1248–1254 (2016).

19.   Weidman, M. C., Nguyen, Q., Smilgies, D. M. & Tisdale, W. A. Impact of Size Dispersity, Ligand Coverage, and Ligand Length on the Structure of PbS Nanocrystal Superlattices. *Chem. Mater.* **30,** 807–816 (2018).

20.   Kaushik, A. P. & Clancy, P. Solvent-driven symmetry of self-assembled nanocrystal superlattices-A computational study. *J. Comput. Chem.* **34,** 523–532 (2013).

21.   Kister, T., Monego, D., Mulvaney, P., Widmer-Cooper, A. & Kraus, T. Colloidal Stability of Apolar Nanoparticles: The Role of Particle Size and Ligand Shell Structure. *ACS Nano* **12,** 5969–5977 (2018).

22.   Boles, M. A., Ling, D., Hyeon, T. & Talapin, D. V. The surface science of nanocrystals. *Nat. Mater.* **15,** 141–153 (2016).

23.   Travesset, A. Binary nanoparticle superlattices of soft-particle systems. *Proc. Natl. Acad. Sci.* **112,** 201504677 (2015).

24.   Horst, N. & Travesset, A. Prediction of binary nanoparticle superlattices from soft potentials. *J. Chem. Phys.* **144,** 014502 (2016).

25.   Schapotschnikow, P. & Vlugt, T. J. H. Understanding interactions between capped nanocrystals: Three-body and chain packing effects. *J. Chem. Phys.* **131,** (2009).

26.   Waltmann, C., Horst, N. & Travesset, A. Capping Ligand Vortices as "Atomic Orbitals" in Nanocrystal Self-Assembly. *ACS Nano* **11,** 11273–11282 (2017).

27.   Luedtke, W. D. & Landman, U. Structure, Dynamics, and Thermodynamics of Passivated Gold Nanocrystallites and Their Assemblies. *J. Phys. Chem.* **100,** 13323–13329 (1996).

28.   Luedtke, W. D. & Landman, U. Structure and Thermodynamics of Self-Assembled Monolayers on Gold Nanocrystallites. *J. Phys. Chem. B* **102,** 6566–6572 (1998).

29.   Landman, U. & Luedtke, W. D. Small is different: energetic, structural, thermal, and mechanical properties of passivated nanocluster assemblies. *Faraday Discuss.* **125,** 1 (2004).

30.   Widmer-Cooper, A. & Geissler, P. Orientational ordering of passivating ligands on CdS nanorods in solution generates strong rod-rod interactions. *Nano Lett.* **14,** 57–65 (2014).

31.   Widmer-Cooper, A. & Geissler, P. L. Ligand-Mediated Interactions between Nanoscale Surfaces Depend Sensitively and Nonlinearly on Temperature, Facet Dimensions, and Ligand Coverage. *ACS Nano* **10,** 1877–1887 (2016).

32.   Yadav, H. O. S., Shrivastav, G., Agarwal, M. & Chakravarty, C. Effective interactions between nanoparticles: Creating temperature-independent solvation environments for self-assembly. *J. Chem. Phys.* **144,** 244901 (2016).

33.   Schapotschnikow, P., Pool, R. & Vlugt, T. J. H. Molecular simulations of interacting nanocrystals. *Nano Lett.* **8,** 2930–4 (2008).

34.   Boles, M. A. & Talapin, D. V. Many-Body Effects in Nanocrystal Superlattices: Departure from Sphere Packing Explains Stability of Binary Phases. *J. Am. Chem. Soc.* **137,** 4494–4502 (2015).

35.   Travesset, A. Topological structure prediction in binary nanoparticle superlattices. *Soft Matter* **13,** 147–157 (2017).

36.   Goodfellow, B. W., Yu, Y., Bosoy, C. A., Smilgies, D. M. & Korgel, B. A. The Role of Ligand Packing Frustration in Body-Centered Cubic (bcc) Superlattices of Colloidal Nanocrystals. *J. Phys. Chem. Lett.* **6,** 2406–2412 (2015).

37.   Waltmann, T., Waltmann, C., Horst, N. & Travesset, A. Many Body Effects and Icosahedral Order in Superlattice Self-Assembly. *J. Am. Chem. Soc.* jacs.8b03895 (2018). doi:10.1021/jacs.8b03895

38.   Marrink, S. J., Risselada, H. J., Yefimov, S., Tieleman, D. P. & de Vries, A. H. The MARTINI Force Field: Coarse Grained Model for Biomolecular Simulations. *J. Phys. Chem. B* **111,** 7812–7824 (2007).

39.   Zherebetskyy, D., Scheele, M., Zhang, Y., Bronstein, N., Thompson, C., Britt, D., Salmeron, M., Alivisatos, P. & Wang, L.-W. Hydroxylation of the surface of PbS nanocrystals passivated with oleic acid. *Science* **344,** 1380–1384 (2014).

40.   Arnarez, C., Uusitalo, J. J., Masman, M. F., Ingólfsson, H. I., de Jong, D. H., Melo, M. N., Periole,

X., de Vries, A. H., Marrink, S. J., Ingo, H. I., Jong, D. H. De, Melo, M. N., Periole, X., Vries, A. H. De & Marrink, S. J. Dry Martini, a Coarse-Grained Force Field for Lipid Membrane Simulations with Implicit Solvent. *J. Chem. Theory Comput.* **11,** 260–275 (2015).

41. Dimitrov, D. I., Milchev, a & Binder, K. Polymer brushes in solvents of variable quality: molecular dynamics simulations using explicit solvent. *J. Chem. Phys.* **127,** 084905 (2007).

42. Agarwal, U. & Escobedo, F. A. Mesophase behaviour of polyhedral particles. *Nat. Mater.* **10,** 230–235 (2011).

43. Gantapara, A. P., De Graaf, J., Van Roij, R. R. & Dijkstra, M. Phase diagram and structural diversity of a family of truncated cubes: Degenerate close-packed structures and vacancy-rich states. *Phys. Rev. Lett.* **111,** 1–5 (2013).

44. Damasceno, P. F., Engel, M. & Glotzer, S. C. Predictive self-assembly of polyhedra into complex structures. *Science* **337,** 453–7 (2012).

45. Henzie, J., Grünwald, M., Widmer-Cooper, A., Geissler, P. L. & Yang, P. Self-assembly of uniform polyhedral silver nanocrystals into densest packings and exotic superlattices. *Nat. Mater.* **11,** 131–7 (2012).

46. Kaushik, A. P. & Clancy, P. Solvent-driven symmetry of self-assembled nanocrystal superlattices - A computational study. *J. Comput. Chem.* **34,** 523–532 (2013).

47. Podsiadlo, P., Krylova, G., Lee, B., Critchley, K., Gosztola, D. J., Talapin, D. V., Ashby, P. D. & Shevchenko, E. V. The Role of Order, Nanocrystal Size, and Capping Ligands in the Collective Mechanical Response of Three-Dimensional Nanocrystal Solids. *J. Am. Chem. Soc.* **132,** 8953–8960 (2010).

48. Tam, E., Podsiadlo, P., Shevchenko, E., Ogletree, D. F., Delplancke-Ogletree, M. P. & Ashby, P. D. Mechanical properties of face-centered cubic supercrystals of nanocrystals. *Nano Lett.* **10,** 2363–2367 (2010).

49. Bealing, C. R., Baumgardner, W. J., Choi, J. J., Hanrath, T. & Hennig, R. G. Predicting nanocrystal shape through consideration of surface-ligand interactions. *ACS Nano* **6,** 2118–27 (2012).

50. Häkkinen, H. The gold–sulfur interface at the nanoscale. *Nat. Chem.* **4,** 443–455 (2012).

51. Rabani, E., Reichman, D. R., Geissler, P. L. & Brus, L. E. Drying-mediated self-assembly of nanoparticles. *Nature* **426,** 271–4 (2003).

52. Plimpton, S. Fast Parallel Algorithms for Short-Range Molecular Dynamics. *J. Comput. Phys.* **117,** 1–19 (1995).

53. Frenkel, D. & Smit, B. *Understanding Molecular Simulation*. (Academic Press, 2002).

54. Meijer, E. J., Frenkel, D., LeSar, R. A. & Ladd, A. J. C. Location of melting point at 300 K of

nitrogen by Monte Carlo simulation. *J. Chem. Phys.* **92,** 7570–7575 (1990).